Sensors and Actuators B 263 (2018) 387–399

Contents lists available at ScienceDirect

Sensors and Actuators B: Chemical

journal homepage: www.elsevier.com/locate/snb

Room temperature NO_2 gas sensor based on porous Co_3O_4 slices/reduced graphene oxide hybrid

Bo Zhang, Ming Cheng, Guannan Liu, Yuan Gao*, Lianjing Zhao, Shan Li, Yipei Wang, Fangmeng Liu, Xishuang Liang, Tong Zhang, Geyu Lu*

State Key Laboratory on Integrated Optoelectronics, College of Electronic Science and Engineering, Jilin University, Changchun 130012, People's Republic of China

ARTICLE INFO

Article history:
Received 16 November 2017
Received in revised form 12 February 2018
Accepted 14 February 2018
Available online 16 February 2018

Keywords:
Reduced graphene oxide
Co_3O_4
Room temperature
Gas sensor
NO_2

ABSTRACT

The porous flake-like Co_3O_4 and Co_3O_4/graphene hybrids with different graphene contents were prepared through a facile two-step method. The field emission scanning electron microscopy (FESEM) and transmission electron microscopy (TEM) characterizations proved the tight adherence of graphene sheets to the surface of porous Co_3O_4 slices. Gas sensors based on the as-synthesized products were then fabricated to explore their potential applications. The results indicated that the optimal hybrid exhibited a response of 26.8% to 5 ppm of NO_2 at room temperature (RT), which was 2.27 times higher than that of undoped Co_3O_4 (100 °C). The hybrid sensor also showed fast response, excellent selectivity, long-term stability and extremely low detection limit toward NO_2 at RT. The significantly enhanced sensing properties to NO_2 could be attributed to larger specific surface area, more chemisorbed oxygen species and the coupling effect between Co_3O_4 and graphene in the hybrid. As we all know, as a typical p-type semiconductor, the gas-sensing properties of Co_3O_4 toward oxidizing gases including NO_2 was rarely reported. We believe that our work could pave the way for the future design of Co_3O_4-based gas sensors for oxidizing gases detection at low or even room temperature.

© 2018 Elsevier B.V. All rights reserved.

1. Introduction

For a long time, gas sensors continuously get the attention of researchers due to their extensive applications in environmental monitoring, disease diagnosis and industrial process control. Up to now, various kinds of metal oxides, including n-type ZnO [1,2], α-Fe_2O_3 [3,4], SnO_2 [5,6], In_2O_3 [7,8], WO_3 [9,10] and p-type CuO [11,12], NiO [13,14], Cr_2O_3 [15,16], Co_3O_4 [17,18] have been extensively investigated as gas-sensing materials owing to their superior stability, low cost, and simplicity in preparation.

Generally, in n-type metal oxide, the adsorption of oxygen which extracts electrons will induce the generation of electron depletion layer (EDL) near the grain surface. The gas responses of n-type metal oxides are determined by the thickness of EDL and chemoresistive variation at the inter-particle contacts. Therefore, the gas response increases considerably when the particle size becomes comparable to, or even smaller than twice of the EDL thickness [1,19–21]. On the contrary, in p-type metal oxide, correspondingly, hole accumulation layer (HAL) is built in virtue of the ionized adsorption of oxygen near the surfaces of primary particles. However, the p-type conduction occurs mainly along the semiconducting shell layers. As a result, the variation of hole concentration by interaction with target gases usually leads to limited gas response [22–25]. As reported, the response of a p-type metal oxide based gas sensor to a given gas equals the square root of that of an n-type metal oxide based gas sensor to the same gas under the premise of the identical morphological configurations and others [24,25]. That is why p-type metal oxide based gas sensors were less investigated compared to n-type counterparts for quite some time. Nevertheless, p-type metal oxides are still considered as potential materials for new chemoresistive gas sensors due to their unique merits and it also appears more meaningful to explore high-performance gas sensors based on p-type semiconductors.

Cobalt (II, III) oxide (Co_3O_4), with a typical cubic spinel structure, is composed of a face-centered cubic arrangement of component ions, where Co^{2+} and Co^{3+} ions occupy one-eighth of the tetrahedral sites and half of the octahedral sites, respectively [26]. As the most representative p-type semiconductor, Co_3O_4 has been extensively applied in various fields including catalysis [27–29], energy storage

* Corresponding authors.
E-mail addresses: gaoyuan@jlu.edu.cn (Y. Gao), lugy@jlu.edu.cn (G. Lu).

https://doi.org/10.1016/j.snb.2018.02.117
0925-4005/© 2018 Elsevier B.V. All rights reserved.

[30], gas sensors [26,31–33] and supercapacitors [34]. With respect to gas sensors, Co_3O_4 has been found to be selectively sensitive to CO and volatile organic compounds (VOCs) on account of its good catalysis for CO combustion [27,28] and selective oxidation of VOCs [28]. In fact, the existing Co_3O_4 based gas sensors usually operate at an elevated temperature above 200 °C [35], which goes against the energy-saving principle of practical application. Moreover, the detection gases of Co_3O_4 sensors highly centralize limited kinds of reducing gases. Scarcely any literatures report its gas-sensing properties to oxidizing gases such as NO_2 and O_3. In particular, NO_2, as a most common hazardous gas, has given rise to many serious problems such as acid rain, photo-chemical smog and respiratory diseases. Therefore, we consider it very essential to explore Co_3O_4 based gas sensors with much broader detection range and lower operating temperature.

Recently, graphene has been considered as an ideal candidate in developing room-temperature NO_2 gas sensors due to its intrinsic large surface area, high electron mobility and excellent conductivity under ambient conditions [36,37]. Graphene oxide (GO) and reduced graphene oxide (rGO), two most important derivatives of graphene, are more practically applied to realize room-temperature gas-sensing in view of their cost-effective mass production and the introduced oxygen functional groups and surface defects, which act as active sites for interaction with gas molecules [38,39]. For example, a novel 3D graphene aerogel-ZnO hybrid was reported by Liu et al. [40], which showed a response of 8% to 50 ppm of NO_2 at RT. Dong et al. [41] prepared the nanosphere-like α-Fe_2O_3 modified rGO nanosheets by a simple hydrothermal method, which exhibited a response of 150.63% to 90 ppm of NO_2 at RT.

In this work, the porous Co_3O_4 slices were successfully synthesized. Moreover, different amount of rGO was doped to Co_3O_4 to obtain a series of Co_3O_4/rGO hybrids. Characterizations such as X-ray diffraction (XRD), field emission scanning electron microscopy (FESEM) and X-ray photoelectron spectroscopy (XPS) were then carried out, proving the successful binding of two individual components. At last, gas sensors were fabricated to test their potential applications. Inspiringly, through the doping of rGO, the hybrid sensors exhibited an enhanced response to NO_2 at lower temperature or even RT compared with undoped Co_3O_4. The optimal hybrid showed a high response of 26.8% to 5 ppm of NO_2 at RT, which was 2.27 times higher than that of undoped sensor. It also displayed fast response, excellent selectivity, long-term stability and low detection limit toward NO_2 at RT.

2. Experimental

2.1. Synthesis of materials

All the chemical reagents were of analytical grade (Beijing Chemical Co., Ltd.) and used as received without further purification. Graphene oxide (GO) was synthesized from natural graphite powder by a modified Hummers method.

A typical process for the synthesis of Co_3O_4/rGO hybrid was illustrated in Scheme 1 and described as follows: Porous Co_3O_4 was obtained by a hydrothermal treatment. In a typical procedure, 3 mmol of Co $(NO_3)_2{\cdot}6H_2O$ was added to 30 mL of deionized water with constant stirring of 30 min to form a homogeneous solution. Then 9 mmol of CO $(NH_2)_2$ was added into the above solution and stirred for another 30 min to mix evenly. At last, the solution was transferred into a 50 mL of Teflon-lined stainless-steel autoclave and the reaction system was kept at 160 °C for 16 h. After being cooled to RT, the resulting precipitate was collected by centrifugation, washed with DI water and absolute ethanol several times. We then froze the product at −40 °C for 12 h and freeze-drying to obtain the rosy powder. After that, the powder was annealed at 600 °C for 2 h with a heating rate of 5 °C min^{-1}. At last, black Co_3O_4 was obtained.

A typical process for the synthesis of the Co_3O_4/rGO hybrid was followed by further treatment. In a typical procedure, 20 mg of the as-prepared black Co_3O_4 powder was added to 20 mL of deionized water under vigorous stirring for 1 h to form a homogeneous solution. Then, 200 μL of GO solution (1 mg/mL) was added slowly to the above solution using a pipette and continuously stirred overnight

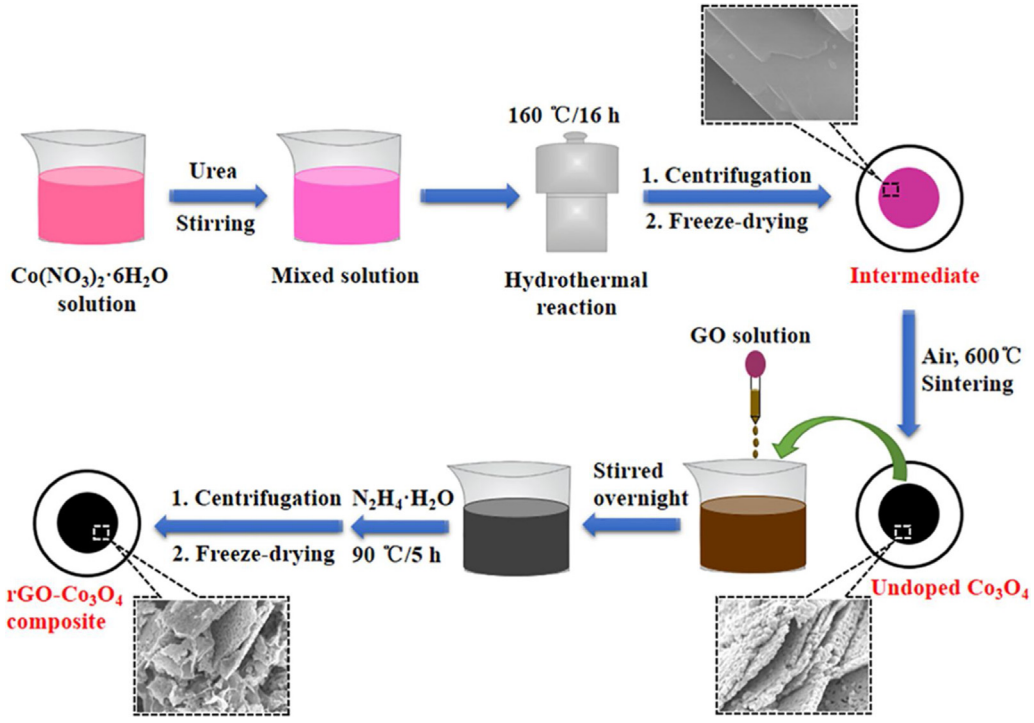

Scheme 1. Schematic illustration of the preparation of porous Co_3O_4 slices/reduced graphene oxide hybrid.

to ensure sufficient binding of graphene sheets and Co_3O_4. Afterwards, 200 μL of $N_2H_4{\cdot}H_2O$ (80%) was added slowly to the mixed solution. At last, the prepared solution was heated in water bath at 90 °C for 5 h. After being cooled to RT, the resulting precipitate was collected by centrifugation, washed with DI water and absolute ethanol several times. We then froze the product at −40 °C for 12 h and freeze-drying to obtain the gloss black powder. After that, the powder was annealed at 500 °C for 1 h under inert atmosphere with a heating rate of 5 °C min^{-1}. Similarly, the hybrids containing other GO amount (500 and 1000 μL of GO solution, 200 μL of $N_2H_4{\cdot}H_2O$) were synthesized using the same procedure, respectively .

The theoretical weight percents of graphene in the as-prepared hybrids were calculated to be 1.0%, 2.4% and 4.7%, respectively. For convenience, hereafter, the hybrids containing 1.0 wt.%, 2.4 wt.% and 4.7 wt.% of graphene will be labeled simply as 1.0% rGO-Co_3O_4, 2.4% rGO-Co_3O_4 and 4.7% rGO-Co_3O_4 throughout the text. Moreover, reduced graphene oxide (rGO) will be called graphene for short. It should also be specially mentioned that 2.4% rGO-Co_3O_4 was found to be most optimal for NO_2 gas sensing applications with regard to sensor response, working temperature, response time and selectivity. Thus, most of the material characterizations of the hybrids were based on 2.4% rGO-Co_3O_4 thereinafter.

2.2. Characterization

X-ray powder diffraction (XRD) analysis was performed on a Rigaku D/max-2550 X-ray diffractometer with high-intensity Cu Kα radiation (λ = 0.154 nm) in the range of 10–75° (2θ). The energy dispersive X-ray spectrometry (EDS) data and field emission scanning electron microscopy (FESEM) images were obtained on a JEOL JSM-7500F microscope operating at 15 kV. Transmission electron microscopy (TEM) and high-resolution transmission electron microscopy (HRTEM) were obtained on a JEOL JEM-2100F microscope with accelerating voltage of 200 kV. Raman spectroscopy analysis was conducted on a RENISHAW INVIA Micro-Raman spectrometer. The X-ray photoelectron spectroscopy (XPS) data were recorded on a PREVAC XPS system. The specific surface area was estimated by the Brunauer–Emmett–Teller (BET) equation based on the nitrogen adsorption isotherm, which was measured with a Micromeritics Gemini VII apparatus (Surface Area and Porosity System) with prior degassing of the product under vacuum at 120 °C overnight.

2.3. Fabrication and measurement of the gas sensor

The sensor fabrication process is described in detail as follows. An appropriate amount of as-prepared powder was mixed with DI water to form a homogeneous paste, and then the paste was coated on an alumina ceramic tube (4 mm in length, 1.2 mm in external diameter, and 0.8 mm in internal diameter), on which a pair of Au electrodes was installed at each end and each electrode was connected with a pair of Pt wires, to form a thick sensing film. After drying in air at RT, the device was then annealed at 200 °C for 2 h to remove the residual water and improve its stability. Then, a Ni-Cr alloy coil was inserted into the alumina ceramic tube as a heater. The operating temperature was controlled by adjusting the heating current that passed through the heater. Finally, the sensor was constructed by connecting the corresponding junctions to the socket of sensor.

The gas-sensing behavior was estimated by a RQ-2 gas-sensing characterization system under laboratory conditions (30% RH, 25 °C). The sensor was placed into an airtight chamber filled with air at the beginning, and then a calculated amount of the test gas was injected into another airtight chamber using an injector. Soon afterward, the sensor was put into this airtight chamber to react with the test gas molecules. After the resistance of the sensor keeping constant for a period of time, the sensor was transferred back into the original airtight chamber filled with air and began to recover. The response of the sensor (P-type) in this work was defined as $(R_a - R_g)/R_a$ to both reducing gases and oxidizing gases. Here, R_a and R_g were the electrical resistance of the gas sensor in air or in the presence of test gases. Moreover, the time taken by 90% resistance variation was defined as the response time or recovery time (τ_{res} or τ_{recov}).

3. Results and discussion

3.1. Structural and morphological characteristics

The structures of all the as-prepared samples were first characterized using XRD, which provided insight into their chemical essence and crystallinity. As shown in Fig. 1 for undoped Co_3O_4, its XRD pattern exhibited very sharp diffraction peaks, indicating the high crystallinity, and all of the recorded diffraction peaks could be well-assigned to the cubic Co_3O_4 phase with lattice constant of a = 8.08 Å, which was in good accordance with those from the standard JCPDS Card No. 9-418. Obviously, the doping of graphene didn't deteriorate the original crystal structure of Co_3O_4 since all the diffraction peaks in the hybrids existed at almost the same 2θ position as that for undoped Co_3O_4. We didn't see obvious damping of the peak intensity, indicating Co_3O_4 maintained the good crystallinity in the hybrids. With the increase of graphene doping amount, the characteristic broad diffraction peak between 23° and 26°, which corresponded to the (002) plane of rGO [42], could also be faintly observed.

The morphologies and microstructures of the unsintered intermediate, undoped Co_3O_4, and 2.4% rGO-Co_3O_4 were analyzed by FESEM and EDS, images of which were shown in Fig. 2. Before sintering, the intermediate exhibited a flake-like morphology, stacking together. In its magnified image (Fig. 2(b)), the flakes of intermediate displayed a very smooth surface. After sintering, however, the randomly stacking Co_3O_4 slices with a porous structure could be seen from Fig. 2(c). In Fig. 2(d), we definitely affirmed this structure, which was beneficial to gas sensing performance by increasing the surface reactive sites and facilitating the diffusion of target gases. We speculated that the holes might generate along with the dehydration and shrink process during the high-temperature sintering. In 2.4% rGO-Co_3O_4, as Fig. 2(e) showed, porous Co_3O_4 slices mixed evenly with a mass of graphene sheets. In Fig. 2(f), the graphene sheets revealed a crumpled, rippled morphology, adhering to the

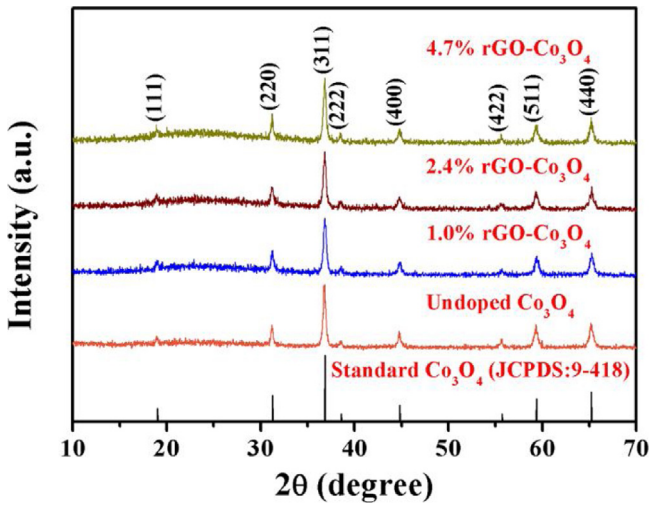

Fig. 1. XRD patterns of the as-prepared undoped Co_3O_4, and graphene-doped hybrids.

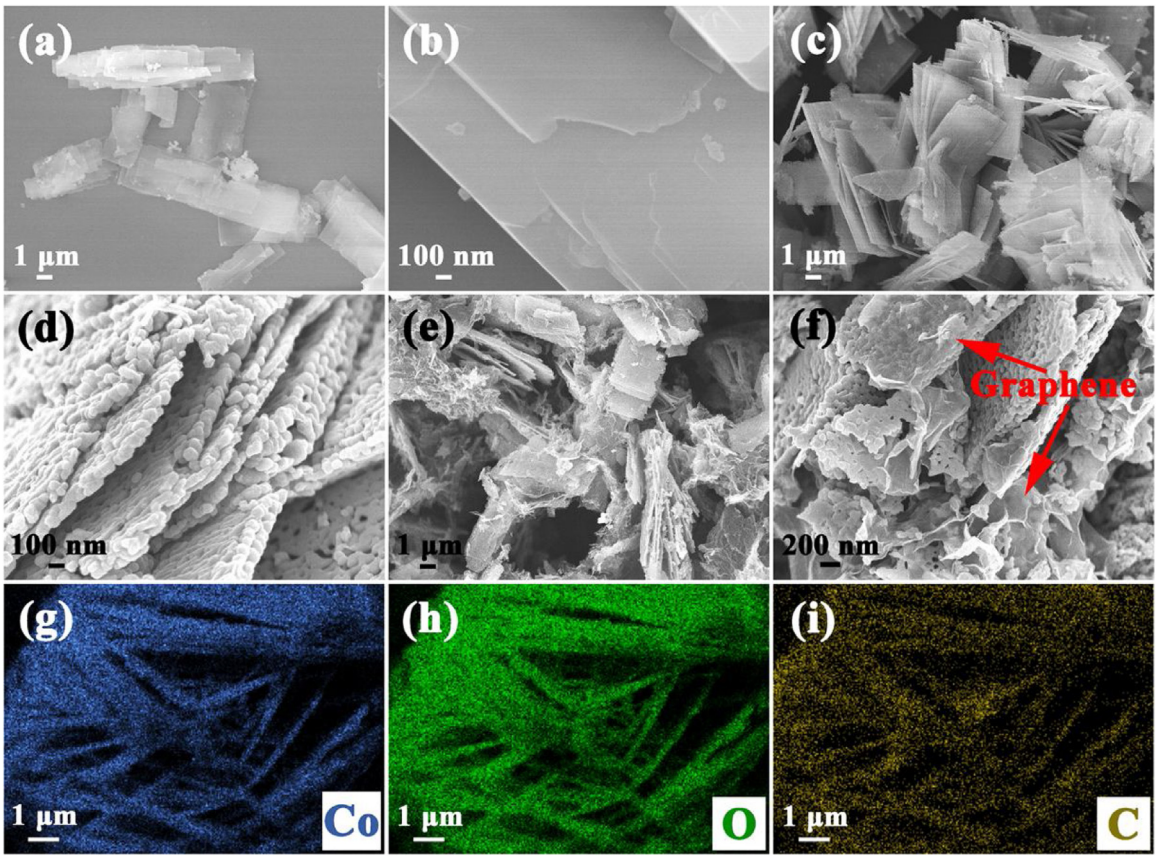

Fig. 2. (a, b) Low- and high-magnification FESEM images of unsintered intermediate. (c, d) Low- and high-magnification FESEM images of undoped Co_3O_4. (e, f) Low- and high-magnification FESEM images of 2.4% rGO-Co_3O_4. (g–i) EDS elemental mapping images of 2.4% rGO-Co_3O_4.

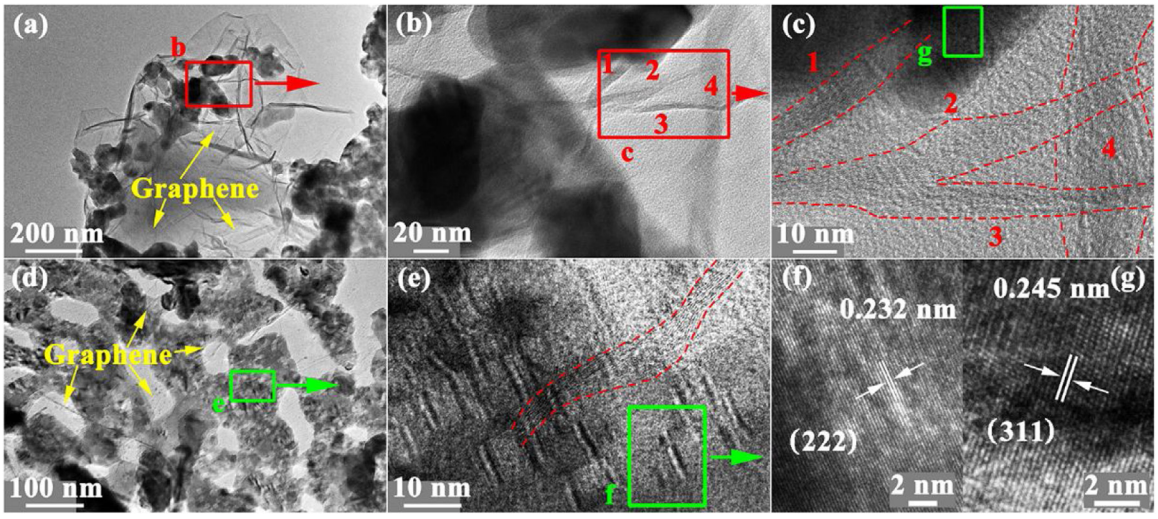

Fig. 3. (a, d) Panoramic TEM images of 2.4% rGO-Co_3O_4. (b, e) Magnified images of the marked regions in (a) and (d), respectively. (c) Magnified image of the marked region in (b). (f, g) HRTEM images of the marked regions in (e) and (c), respectively.

surface of porous Co_3O_4 slices tightly. In addition, graphene in Fig. 2(f) combined with Co_3O_4 slices in many forms, such as gluing, overlapping and encapsulating, which indicated the successful doping of graphene to form Co_3O_4/graphene hybrid. At last, the EDS elemental mapping images of 2.4% rGO-Co_3O_4 was provided to confirm its composition and the spatial distribution of the elements. Obviously, as shown in Fig. 2(g)–(i), Co, O and C were expectedly detected as the three main elements existing in the hybrid. It was also worth mentioning that C element distributed uniformly in the hybrid, which corresponded to the observation in Fig. 2(e).

In order to acquire more-detailed structural and crystalline information of the as-prepared samples, TEM and corresponding HRTEM were also carried out. Two panoramic regions were selected randomly, shown in Fig. 3(a) and (d). In Fig. 3(a), a large piece of graphene wrapped some fragmental Co_3O_4 particles, exhibiting a very tight combination, which kept accordance with the above FESEM observations (Fig. 2(f)). The graphene sheet here was trans-

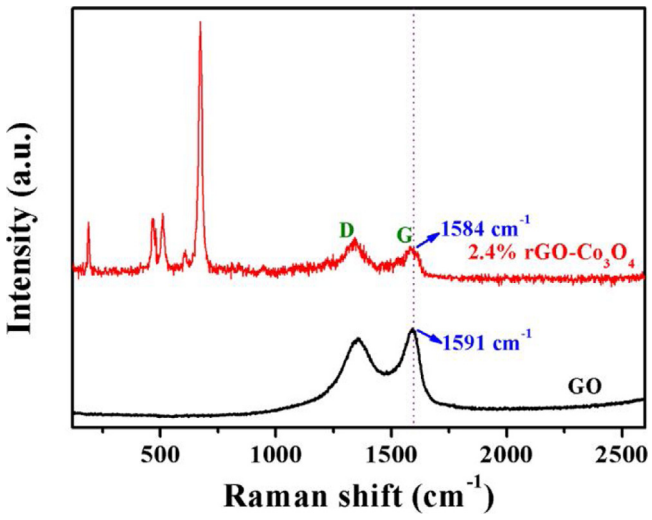

Fig. 4. Raman spectra of GO and 2.4% rGO-Co_3O_4.

parent, frizzy, and quite plicated, indicating its extreme thinness and the successful intercalation by Co_3O_4 particles. Similarly, in Fig. 3(d), the uniform mixture of graphene and Co_3O_4 could be observed. However, unlike the broken fragments in Fig. 3(a), the selected hybrid in Fig. 3(d) was comparatively intact. The graphene sheets covered or attached the surface of porous Co_3O_4 slice. We could catch sight of the permeable holes distributing in Co_3O_4 surface, corresponding to Fig. 2(d). As shown in Fig. 3(c), Co_3O_4 grains with a well crystalline texture were surrounded by graphene sheets, which displayed a characteristic curving lattice-fringed structure. Analogously, in Fig. 3(e), we could also see the clear curving lattice fringe of graphene. The HRTEM images of Fig. 3(f) and (g), which corresponded to the marked areas in Fig. 3(e) and (c), showed the fringe spacing of 0.232 and 0.245 nm, respectively, agreeing well with the spacing of the (222) and (311) lattice planes of the cubic Co_3O_4 phase.

Fig. 4 showed the Raman spectra of undoped Co_3O_4 and 2.4% rGO-Co_3O_4. We could see two common peaks in both spectra, namely the D band and G band, which were characteristic peaks of carbon materials [43]. The G band was characteristic of pristine graphene. Differently, the D band was usually assigned to local defects and disorders especially at the edges of graphite platelets [43]. In the spectra of 2.4% rGO-Co_3O_4, the G band ($\sim$1584 cm^{-1}) was much closer to graphite ($\sim$1580 cm^{-1}) compared with GO spectra ($\sim$1591 cm^{-1}). The red shift of the G band of 2.4% rGO-Co_3O_4 indicated the restoration of the conjugated π systems during the hydrothermal reaction, namely the successful reduction of GO. Moreover, the increased I_D/I_G intensity ratio of 2.4% rGO-Co_3O_4 ($\sim$1.17) compared with that of GO ($\sim$0.91) demonstrated a decrease in the average size of the sp^2 domains after reduction of GO, which generated a stronger D band signal.

The elemental compositions and chemical states of undoped Co_3O_4 and 2.4% rGO-Co_3O_4 were further determined using XPS spectra as shown in Fig. 5. The sharp peaks in the full scan spectra revealed the presence of carbon, oxygen and cobalt elements in 2.4% rGO-Co_3O_4 (Fig. 5(a)). To further understand the electronic states of the elements, high-resolution spectra were recorded. The core level spectrum of Co 2p were analyzed using peak fit and deconvolution. As shown in Fig. 5(b), the high resolution spectrum of Co 2p exhibited two characteristic peaks and corresponding satellite peaks. The two major characteristic peaks with binding energies at 779.7 and 794.8 eV corresponded to Co $2p_{3/2}$ and Co $2p_{1/2}$, respectively [44,45]. The energy gap between the two peaks was about 15.1 eV (spin orbit splitting), indicating the existence of both Co^{2+}/Co^{3+} species [46], which was also embodied clearly in Fig. 5(b). The presence of the two shakeup satellite peaks located above the two main peaks (789.4 and 804.2 eV) further confirmed the formation of Co_3O_4 crystal phase [47].

A deconvoluted C 1s core level spectrum usually provides evidence for the removal of the oxygen groups and the formation of graphene. As shown in Fig. 5(c), five different peaks centered at 284.6, 285.6, 286.7, 288.0 and 289.0 eV were observed in the C 1s deconvolution spectrum of GO, corresponding to C=C/C—C in aromatic rings, C—OH (hydroxyl groups), C—O—C (epoxy groups), C=O (carbonyl groups), and O—C=O (carboxyl groups), respectively [41]. For 2.4% rGO-Co_3O_4 (Fig. 5(d)), the intensities of most C 1s peaks, especially the peak assigned to C—O—C (epoxy groups), decreased a lot, indicating considerable de-oxygenation during the reduction process.

The ability of the sensing materials to absorb and ionize oxygen species was fundamental to the performances of gas sensors. To verify the status of oxygen species of the as-prepared products, a deconvoluted O 1s core level spectrum of undoped Co_3O_4 and 2.4% rGO-Co_3O_4 were also conducted. The high resolution XPS spectra of O 1s in Fig. 5(e) and (f) could be classified to three Gaussian function peaks, which corresponded to three kinds of oxygen species on the materials' surface. The first peak was O_L component, attributed to the lattice oxygen species (Co—O). The second peak was O_V component in oxygen vacancy regions, and the third peak (O_C component) was identified to chemisorbed and dissociated oxygen species [48]. It's worth noting that the same component peak in Co_3O_4 and 2.4% rGO-Co_3O_4 located at a different binding energy, indicating an interaction between graphene and Co_3O_4 and the close bonding between them. We also listed the center positions and the relative percentages of each peak in Table 1. By contrast, obviously, the percentage of O_L component of 2.4% rGO-Co_3O_4 decreased dramatically compared with undoped Co_3O_4. Consequentially, O_V and O_C components occupied a higher percentage in the case of 2.4% rGO-Co_3O_4. Generally, as we know, O_L was attributed to the oxygen ions in the crystal lattice which was thought to be very stable and had no contribution to the gas response. The increase of O_V component indicated more defects and active sites existing in 2.4% rGO-Co_3O_4, which was advantageous for the gas adsorption and reaction. The increase of O_C component in 2.4% rGO-Co_3O_4 meant that more surface chemisorbed oxygen species could participate in the surface oxidation-reduction reactions, thus causing a larger change in sensor resistance. Therefore, through the doping of graphene, the hybrid had more defects and possessed a stronger ability for adsorbing the ionized oxygen species, also contribut-

Table 1
Fitting results of O 1s XPS spectra of undoped Co_3O_4 and 2.4% rGO-Co_3O_4.

Materials	Oxygen species	Binding energy (eV)	Relative percentage (%)
undoped Co_3O_4	O_L(Co—O)	529.5	71.23
	O_V(vacancy)	530.74	20.61
	O_C(chemisorbed)	532.03	8.16
2.4% rGO-Co_3O_4	O_L(Co—O)	529.7	43.72
	O_V(vacancy)	530.99	24.73
	O_C(chemisorbed)	532.38	31.55

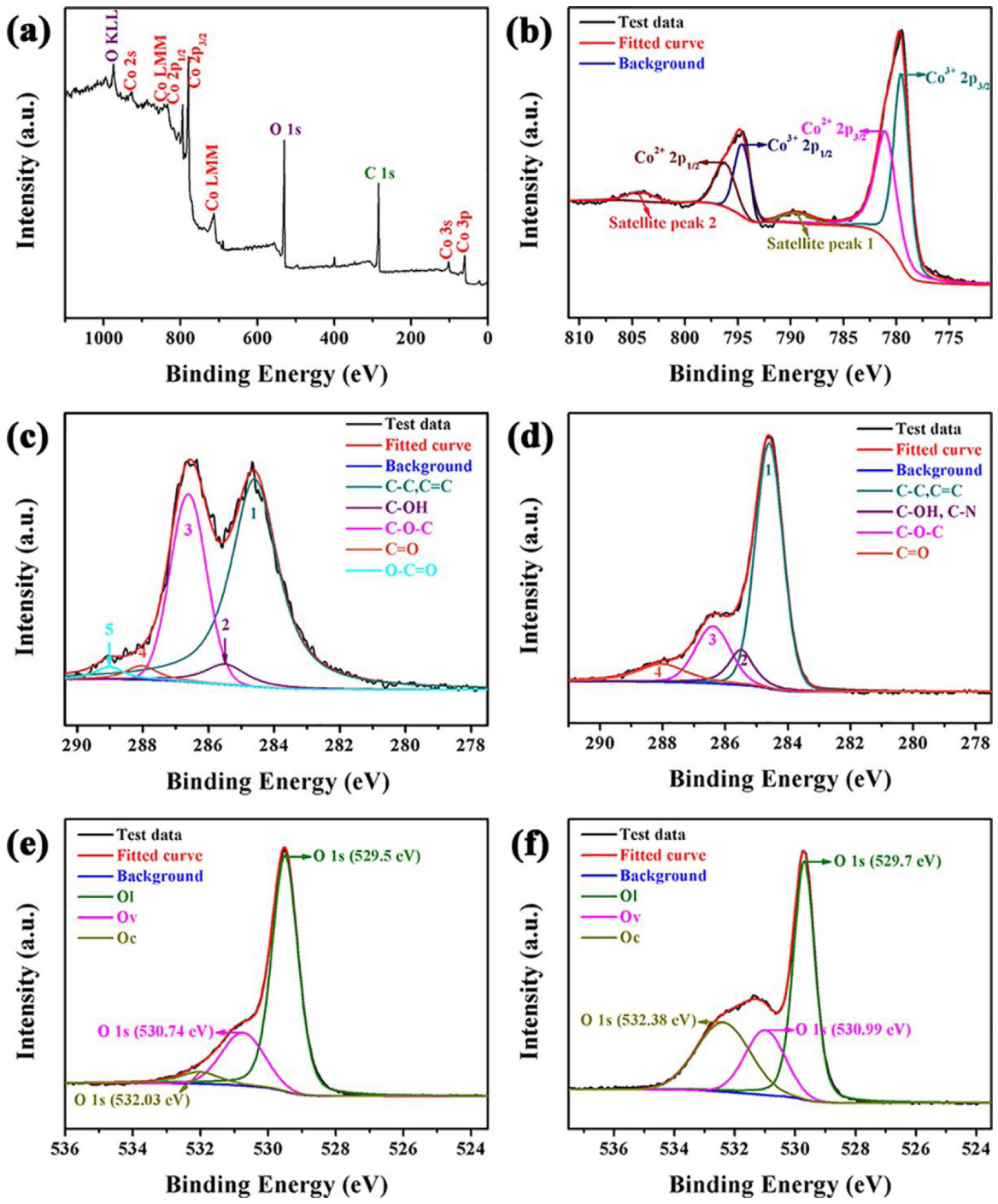

Fig. 5. (a) Wide scan XPS spectra of 2.4% rGO-Co_3O_4. (b) The high-resolution spectrum of Co 2p peak in 2.4% rGO-Co_3O_4. (c, d) XPS C 1s core level spectra of GO and 2.4% rGO-Co_3O_4. (e, f) XPS O 1s core level spectra of undoped Co_3O_4 and 2.4% rGO-Co_3O_4.

ing to its probable high-performance gas-sensing properties when used as gas-sensing materials.

As we know, the specific surface area is one of the most significant parameters for gas sensing materials. On account of the intrinsic high specific surface area of graphene, deservedly, we can speculate that the doping of graphene to Co_3O_4 may lead to a hybrid with higher specific surface area. The BET surface area of the as-prepared samples were investigated based on nitrogen adsorption-desorption isotherms, as shown in Fig. S1 in Supplementary Material. The BET surface areas of undoped Co_3O_4, 1.0% rGO-Co_3O_4, 2.4% rGO-Co_3O_4 and 4.7% rGO-Co_3O_4 were calculated to be 9.93, 15.96, 18.03 and 20.64 $m^2\ g^{-1}$, respectively. On the basis of above results, although very little concentration, the doping of graphene still increased the specific surface area of Co_3O_4 a lot.

Based on above results, more chemical adsorbed oxygen and higher specific surface area observed in hybrids with doping of graphene, we could affirm it was beneficial to enhance gas sensing properties owing to the elevated active sites when exposed to the target gas atmosphere.

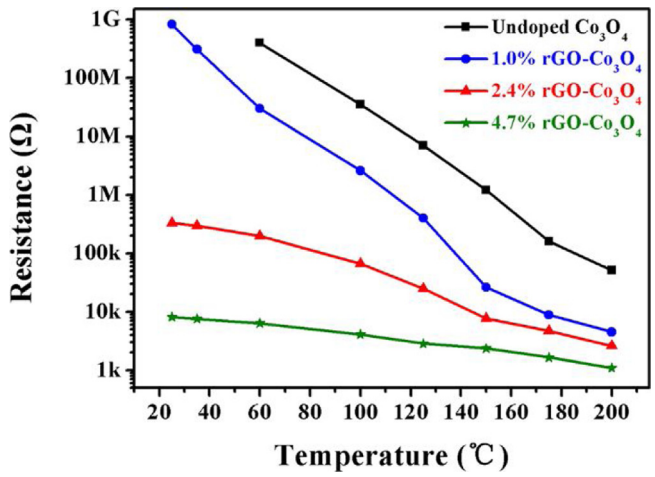

Fig. 6. The resistance variation of undoped Co_3O_4 and all the as-prepared hybrids versus operating temperature.

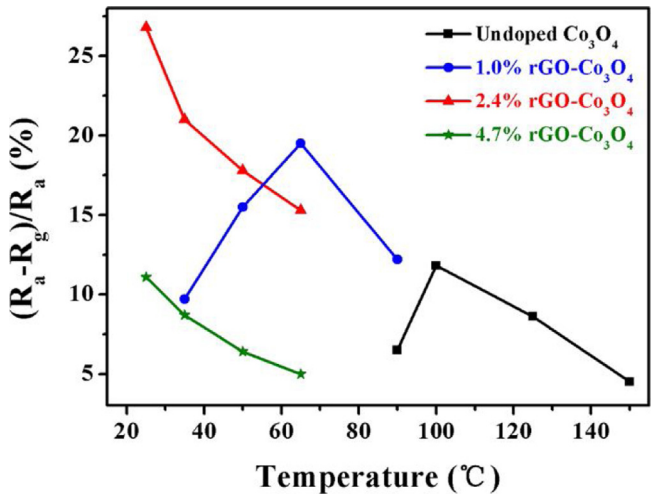

Fig. 7. Correlation between gas responses to 5 ppm of NO_2 and the operating temperature for the sensors fabricated from the as-obtained samples.

3.2. Gas-sensing performances

We first tested the resistance variation of undoped Co_3O_4 and all the as-prepared hybrids with temperature increasing. As shown in Fig. 6, the resistances of all the samples decreased sharply versus temperature increase. The resistance of undoped Co_3O_4 below 60 °C was not provided because it was over the measuring range of the instrument (1 GΩ). In addition, the resistances of the hybrids were much lower than undoped Co_3O_4 by orders of magnitude and that under the same temperature, the larger the graphene doping amount, the smaller the hybrid's resistance was. This was probably given rise to by the excellent electrical conductivity of graphene. Therefore, the doping of graphene could greatly improve the electrical properties of Co_3O_4 and lower its resistance to a large extent, making the room-temperature detection of the target gas possible.

To explore the advantages of graphene-doping hybrids, all the as-prepared products were used as gas-sensing materials to study their properties. For metal oxide based gas sensors, both the operating temperature and dopant amount have great influences on their gas sensing properties. Fig. 7 showed the responses of the gas sensors based on undoped Co_3O_4 and all the prepared hybrids to 5 ppm of NO_2 measured at the temperature range of 25–150 °C aiming to determine the optimum operating temperature and the optimum graphene doping amount. Obviously, the NO_2 responses of undoped Co_3O_4 and 1.0% rGO-Co_3O_4 exhibited a common "volcano" shape. Differently, the NO_2 responses of 2.4% rGO-Co_3O_4 and 4.7% rGO-Co_3O_4 exhibited a distinct feature, decreasing with temperature increase and seemingly more suitable for low temperature detection. The sensor based on undoped Co_3O_4 had a response of 11.8% to 5 ppm of NO_2 and the maximum response appeared at 100 °C, while the sensors based on 1.0% rGO-Co_3O_4 and 2.4% rGO-Co_3O_4 showed enhanced responses of 19.5% and 26.8% to 5 ppm of NO_2 at much lower optimum operating temperature of 65 and 25 °C, respectively. Though the optimal working temperature of 4.7% rGO-Co_3O_4 was also RT, its response to NO_2 was even slightly lower than undoped Co_3O_4. Therefore, based on the above analysis, we concluded that the appropriate graphene doping amount could greatly reduce the optimal working temperature of Co_3O_4 and enhance its response to NO_2 at the same time. Nevertheless, it's not that the more graphene doping amount the better. This could be partially attributed to the excessive coverage of the Co_3O_4 surface caused by graphene, which would decrease the utility factor of the sensing body. Accordingly, among the as-synthesized products, taking both gas response and optimal working temperature for consideration, 2.4 wt.% of graphene was considered as the optimum doping amount and thus the hybrid of 2.4% rGO-Co_3O_4 was chosen to further investigate other gas-sensing properties.

In order to observe the impact of graphene doping on the response-recovery properties, we listed the response transients of the sensors based on the as-obtained samples to 5 ppm of NO_2 at their respective optimal working temperature. As shown in Fig. 8(a)–(d), identically, for all the four sensors, the resistance decreased upon exposure to oxidizing NO_2, which was consistent with the p-type gas sensing behavior of both Co_3O_4 and rGO. Specifically, the undoped Co_3O_4 sensor exhibited a short response time of 3.5 min and the resistance of the sensor could even recover to the initial value within 1 min. The fast response and recovery speed of the undoped Co_3O_4 sensor could be attributed to the following factors. Firstly, the porous structure of Co_3O_4 slices was very advantageous to the adsorption, diffusion and desorption process of NO_2 molecules. Secondly, the high working temperature (100 °C) also played a key role. After the doping of graphene, the response time for 1.0% rGO-Co_3O_4, 2.4% rGO-Co_3O_4 and 4.7% rGO-Co_3O_4 was 4.5, 1.5 and 2.2 min, respectively. When the doping amount of graphene was low, 1.0% rGO-Co_3O_4 for example, its promotion effect to the sensor's response speed (excellent mobility of charge carriers in graphene) couldn't counteract the adverse impact of the decrease of working temperature (from 100 to 65 °C). Therefore, its response time was longer. When the doping amount was high, though under RT, the 2.4% rGO-Co_3O_4 and 4.7% rGO-Co_3O_4 sensors displayed a much faster response speed. It's also worth mentioning that the 2.4% rGO-Co_3O_4 sensor not only responded the fastest but also had the highest response to NO_2 among the four sensors, which further indicated the importance of the appropriate graphene doping amount. However, though having a faster response speed, the sensors based on the hybrids all exhibited a very long desorption process of NO_2. The long recovery of graphene-containing sensors to NO_2 gas had been reported extensively [49–53], which might be attributed to close bonding of the NO_2 molecules with the residual oxygen functional groups existing on rGO surface [38].

It could be observed in Fig. 9(a) and (b) that the sensor response increased with the increase of NO_2 concentration. When stacking the individual response-recovery curve together in a commonable abscissa, as shown in Fig. 9(c) and (d), we found that the sensor responded faster to a higher NO_2 concentration. Fig. 9(e) showed the sensor response vs NO_2 concentration at RT. We noticed that the response of the 2.4% rGO-Co_3O_4 sensor to 50 ppb of NO_2 could still reach 3.3%, which indicated the extremely low detection limit of the sensor.

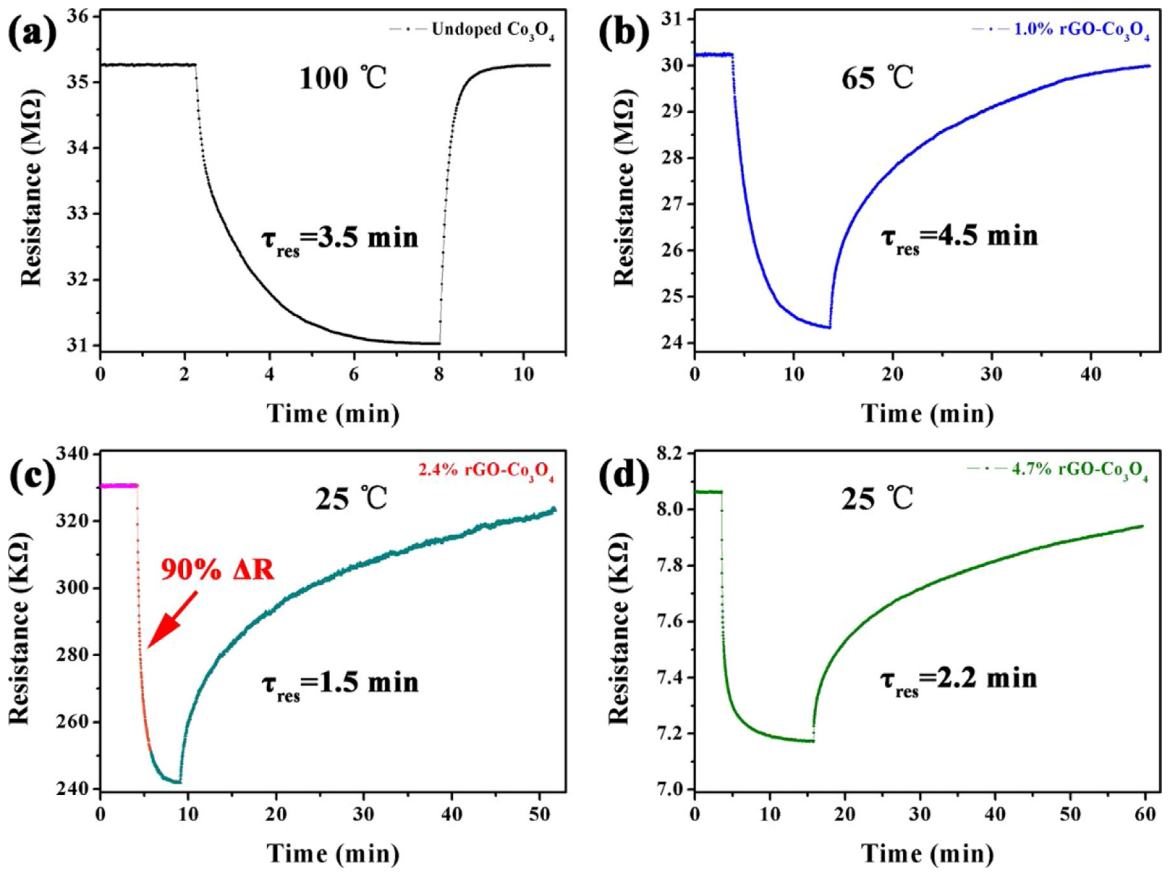

Fig. 8. (a–d) The response transients of the sensors based on undoped Co_3O_4, 1.0% rGO-Co_3O_4, 2.4% rGO-Co_3O_4 and 4.7% rGO-Co_3O_4 to 5 ppm of NO_2 at their respective optimal operating temperature.

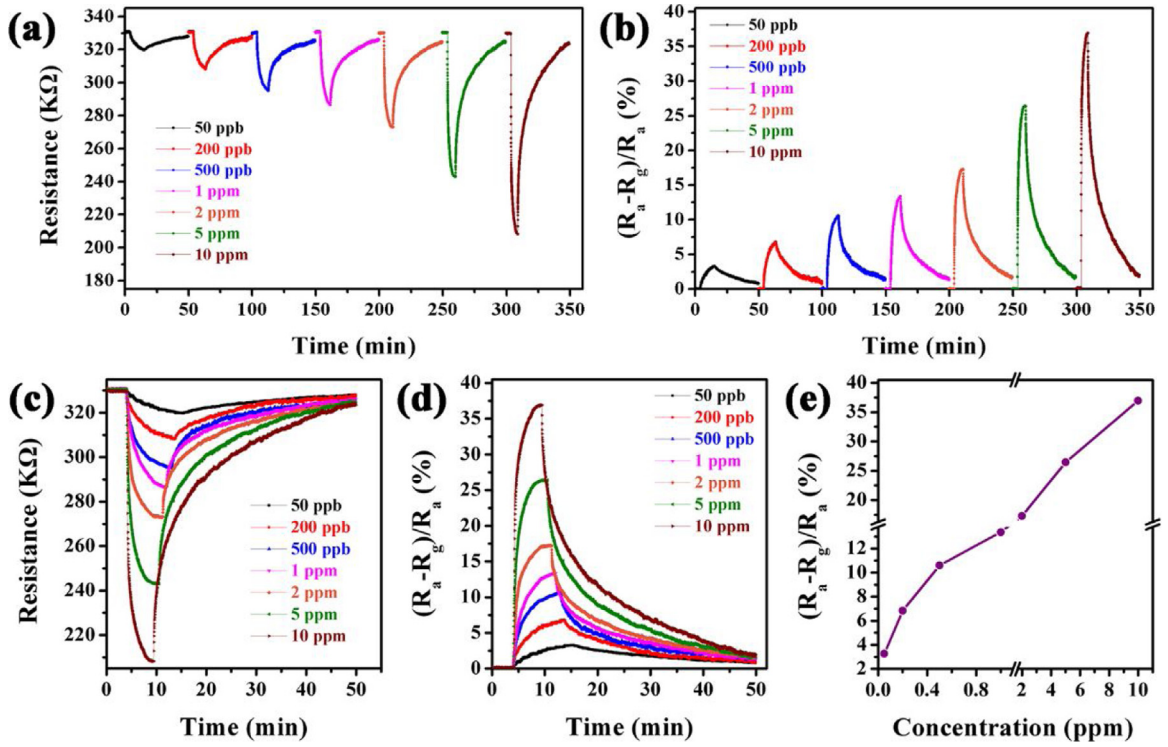

Fig. 9. (a, b) The dynamic resistance and corresponding response variation curves of the sensor based on 2.4% rGO-Co_3O_4 when orderly exposed to NO_2 with increasing concentration at RT. (c, d) The response transients of the sensor based on 2.4% rGO-Co_3O_4 to different concentrations of NO_2 at RT in the same abscissa. (e) The response value of the 2.4% rGO-Co_3O_4 sensor vs NO_2 concentration at RT.

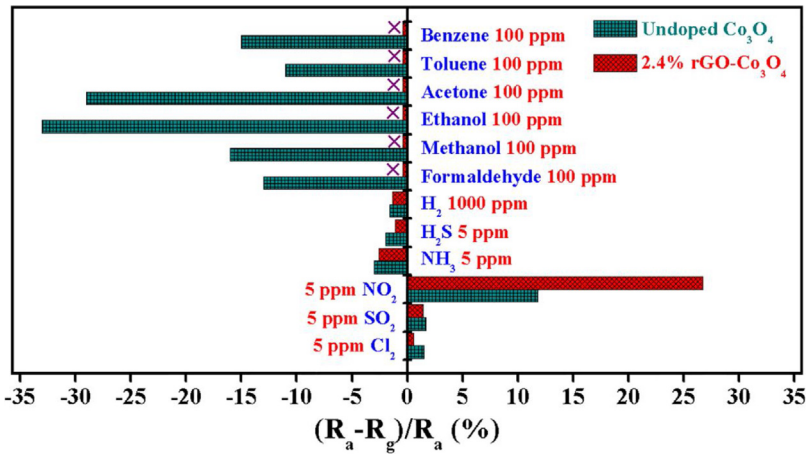

Fig. 10. Responses of the sensors based on undoped Co_3O_4 and 2.4% rGO-Co_3O_4 to various test gases at their respective optimal operating temperature.

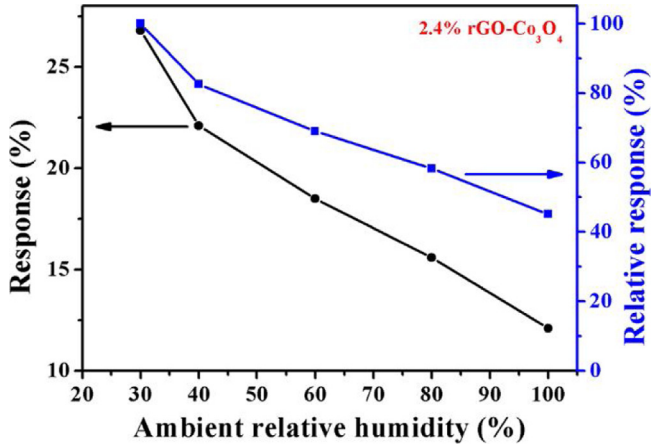

Fig. 11. The response variation of the sensor based on 2.4% rGO-Co_3O_4 to 5 ppm of NO_2 at RT with increasing ambient relative humidity (RH).

Since selectivity is a remarkable aspect of sensing properties, the responses of undoped Co_3O_4 and 2.4% rGO-Co_3O_4 based gas sensors to various kinds of test gases (such as NO_2, H_2S, NH_3, acetone, ethanol, formaldehyde and so on) at 100 and 25 °C were tested. As shown in Fig. 10, the sensor based on 2.4% rGO-Co_3O_4 exhibited decreased responses for most test gases but increased response only to the target NO_2 compared to the undoped Co_3O_4 sensor. In addition, the 2.4% rGO-Co_3O_4 sensor displayed the highest response to NO_2 and the value of which was about 10.5–48.5 times higher than that of other test gases (exclusive of VOCs), while the ratio was only about 3.9–7.7 for the undoped Co_3O_4 sensor. The sensor based on undoped Co_3O_4 could exhibit visible responses to 100 ppm of VOCs at 100 °C (no obvious responses to VOCs of 5 ppm). However, at RT, the 2.4% rGO-Co_3O_4 sensor didn't show any responses to VOCs, probably due to the required high activation energy barrier of the reactions between VOCs and semiconductor's surface. Based on the results, the doping of graphene greatly promoted the tendentious response of NO_2 and thus the sensor based on 2.4% rGO-Co_3O_4 exhibited a much better selectivity toward NO_2 compared with the undoped Co_3O_4 sensor.

The response of 2.4% rGO-Co_3O_4 sensor to NO_2 gas with the presence of moisture was also recorded and shown in Fig. 11. The relative humidity (RH) range we adopted was 30%–100% and we defined the sensor response at 30% (26.8%) as the standard value (100%). As we can see, the moisture was disadvantageous to the sensor response and it attenuated more than 50% of its initial value when the relative humidity reached 100%.

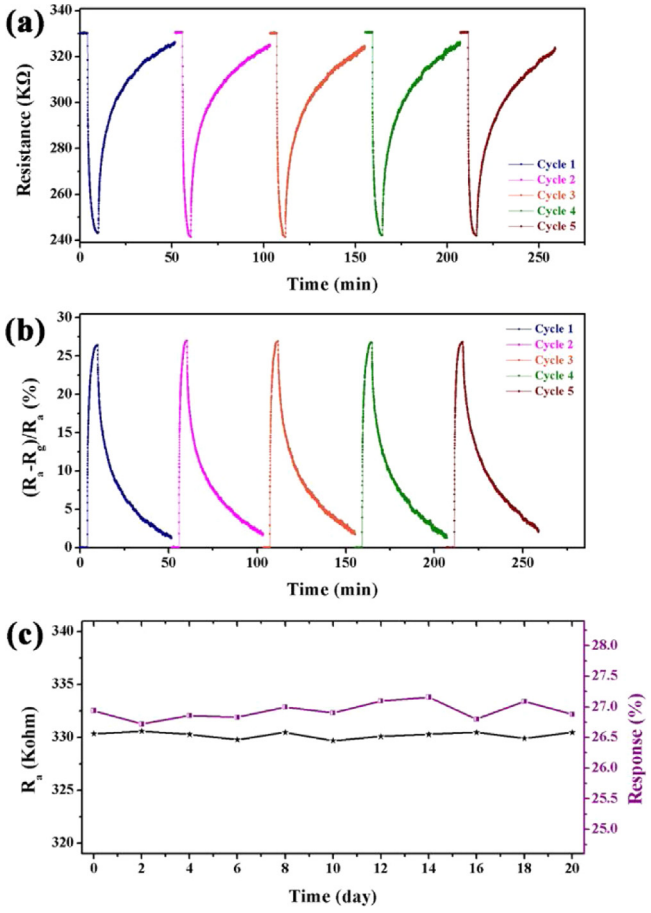

Fig. 12. (a, b) Repeatability and (c) long-term stability of the gas sensor based on 2.4% rGO-Co_3O_4 at RT.

It is well-known that the repeatability and long-term stability are vitally important parameters for sensor devices from the perspective of practical application. As illustrated in Fig. 12(a) and (b), for the 2.4% rGO-Co_3O_4 sensor, its continuous response-recovery curves of resistance and response variations to 5 ppm of NO_2 at RT maintained the initial amplitude without a clear attenuation upon 5 cycles, which revealed the sensor's stable and repeatable character. In addition, the continuous measurement of the response values of the 2.4% rGO-Co_3O_4 sensor to 5 ppm of NO_2 at RT and also its resis-

Table 2
Comparison of NO_2 sensing performances of the current work with other reported literatures.

Materials	Conc. (ppm)	Temp. (°C)	Response	$\tau_{res.}/\tau_{recov.}$ (min)	Detection limit (ppm)	Ref.
SnS_2	10	120	36.33[a]	2.83/2.33	0.6	[54]
MoS_2	1	200	5.8[a]	41/39	0.02	[55]
MoS_2	100	RT (UV)	35.16%[b]	0.48/5.83	5	[56]
ZnO	40	290	264[a]	0.12/0.58	25	[57]
ZnO/CNT	1000	150	9.7[a]	1.17/1.67	50	[58]
WO_3	1	300	53.9[a]	–/–	0.5	[59]
PdO-Co_3O_4	20	100	44.11%[c]	–/–	1	[60]
Au/CuO	5	300	90%[c]	–/–	1	[61]
rGO	100	RT	1.41[d]	15/35	–	[50]
ZnO/rGO	50	RT	8%[b]	2.2/2.73	10	[40]
α-Fe_2O_3/rGO	90	RT	150.63%[c]	–/–	0.18	[41]
Fe_3O_4/rGO	400	RT	24.2%[c]	4.58/12.3	30	[42]
Co_3O_4/rGO	60	RT	80%[c]	–/–	–	[52]
WO_3/rGO	56	RT	40.8%[e]	–/–	7	[62]
SnO_2/rGO	50	RT	6.5%[b]	3.17/3.73	10	[63]
2.4% rGO-Co_3O_4	5	RT	26.8%[c]	1.5/40	0.05	This work

Conc.: Gas concentration; Temp.: Operating temperature; $\tau_{res.}/\tau_{recov.}$: Response/recovery time.
[a] R_g/R_a.
[b] $(R_g - R_a)/R_a$.
[c] $(R_a - R_g)/R_a$.
[d] $(G_g - G_a)/G_a$.
[e] $(I_g - I_a)/I_a$.

tance in air atmosphere (R_a) for 20 days in Fig. 12(c) further verified its excellent long-term stability.

In addition, a comparison between the sensing performances of the sensor fabricated in our work and literature reports [40–42,50,52,54–63] were summarized in Table 2. Through comparison with different kinds of sensing materials selective to NO_2, we are conscious of both the superiority and inferiority of the prepared rGO-Co_3O_4 hybrid in the present work. As we can see, for single metal sulfides and oxides or their composites with noble metals, they can exhibit much elevated response at high operating temperature, accompanied by fast response and recovery process. For rGO based materials, they can generally exhibit response to NO_2 at low or even room temperature. However, the responses are generally very low and they can only detect high concentration of NO_2. Accordingly, the low working temperature and detection limit in the present work are satisfying. In the future work, we will focus on solving the long response and recovery time in rGO-based sensing materials when detecting NO_2 at low or even room temperature.

3.3. Gas-sensing mechanism

Generally, for p-type semiconductor oxides, Co_3O_4 for example, the accepted gas-sensing mechanism can be described as follows. It involves resistance changes induced by the chemisorption of oxygen adions and reactions of the gas molecules on the surface of the sensing materials. In general, when exposed to air, oxygen molecules will be adsorbed onto the surfaces of as-obtained Co_3O_4 and ionize into species such as O_2^- (below 100 °C), O^- (100–300 °C) and O^{2-} (above 300 °C) [64] by transferring holes to the valence band of the p-type semiconductor, thus increasing the hole concentration and decreasing the sensor resistance. The adsorption of the oxygen molecules will cause the formation of the hole accumulation layer (HAL) on the surface of Co_3O_4. Upon exposure to oxidizing NO_2 gas at low or even RT, due to its high electron affinity, NO_2 molecules could be directly adsorbed onto the surface of Co_3O_4 by extracting electrons from the conduction band (Eq. (1)). In addition, NO_2 molecules could react with the chemisorbed O_2^- on the surface forming adsorbed $NO_3^-{}_{(ads)}$ (Eq. (2)), which will cause the increase of the accumulation width and lower the resistance of the sensor [65].

$$NO_{2(gas)} + e^- \rightarrow NO_2^-{}_{(ads)}; \quad (1)$$

$$2NO_{2(gas)} + O_2^-{}_{(ads)} + e^- \rightarrow 2NO_3^-{}_{(ads)}. \quad (2)$$

When Co_3O_4 was doped by p-type rGO, isotype p-p heterointerfaces between p-type Co_3O_4 and p-type rGO with different work functions would generate. In general, heterojunctions formed in sensing materials could account for the enhancement of gas response by promoting the adsorption of target gases (chemical sensitization) or resistance modulation (electronic sensitization) [66]. Different from p–n heterojunctions, where recombination between majority charge carriers occurs and the total number of charge carriers is decreased, isotype heterojunctions can result in spatially separated charge carriers with the total number of charge carriers unchanged.

The work function (Φ) of Co_3O_4 was reported as 6.1 eV [67]. For rGO, due to different kinds of functional groups on its surface, its work function varied from 4.2–6.8 eV [68]. Combined with the much decreased resistance values of obtained rGO-Co_3O_4 hybrids in this work, we speculated that Φ_{rGO} exceeded Φ_{Co3O4}. As a result, electrons would flow from Co_3O_4 to rGO until the fermi energy levels of the two materials became the same across the heterojunctions, which caused a thicker HAL around the surface of Co_3O_4 and the trapping of electrons in isolated rGO sheets [69]. Moreover, the conductivity of rGO is much better than that of Co_3O_4. Thus, the increase of rGO concentration could cause a decrease in the conductivity of rGO-Co_3O_4 hybrids both by establishing p-p heterojunctions and by increasing the portion of the conductive phase.

The spatially separated charge carriers caused by p-p heterojunctions would lead to additional modulation of the total resistance of the sensor, thus the enhanced sensing response. In the hybrid, vacancies, defects and oxygen functional groups on rGO plane could act as active sites for interaction with NO_2 molecules [38]. Therefore, NO_2 molecules could react with chemisorbed oxygen species not only on Co_3O_4 surface but only on the plain of rGO sheets. As a result, the trapped electrons that were transferred from Co_3O_4 and stored in the rGO sheets were withdrawn upon exposure to oxidizing NO_2, thereby restoring the hole concentration of the hybrid and decreasing its resistance. Moreover, the increase of O_C component in the hybrid indicated that more surface chemisorbed oxygen species could participate in the surface oxidation-reduction reactions. As a result, more electrons would be extracted by NO_2 molecules, further inducing the increase of hole concentration and larger sensor response.

Furthermore, the synergetic coupling effect between Co_3O_4 and graphene were often mentioned when involving their hybrids [52,70]. As mentioned in Fig. 5, the different peak positions of oxygen species of Co_3O_4 and 2.4% rGO-Co_3O_4 had proved the successful formation of interfacial Co—O—C bonding in the hybrid. Co cations in Co_3O_4 were electrostatically attracted by originally covalently bonded oxygen atoms in oxygen-containing groups of graphene matrix. Due to the large electronegativity of oxygen atoms, the generated coupling Co-O bonding became more ionic. As a result, the Co^{3+} or Co^{2+} centers would serve as the extra activity sites for NO_2 molecules. Then, electrons could be extracted indirectly from the p-type graphene through the bridging oxygen ions, leading to the extra increase of hole concentration of the hybrid and enhanced sensor response.

However, as mentioned above, it's not that the more graphene doping amount the better. We can see that the resistance of 4.7% rGO-Co_3O_4 (Fig. 6) was decreased dramatically to only 8.06 kΩ at RT, very close to a conductor. The much lower resistance would greatly suppress the resistance modulation. Moreover, too much rGO sheets would also cover the active sites on Co_3O_4 surface and decrease the utility factor of the sensing body.

The sensor based on 2.4% rGO-Co_3O_4 hybrid in this work also exhibited excellent tendentious selectivity toward NO_2, which couldn't be interpreted through increased chemisorbed oxygen species or the formation of isotype p-p heterojunctions. Generally speaking, the selectivity of the sensor is influenced by several factors such as the LUMO (lowest unoccupied molecule orbit) energy of gas molecules, the amount of gas adsorption on the sensing material, and the different operating temperature [71,72]. Customarily, VOCs, like acetone and ethanol, need high temperature to react with the chemisorbed oxygen species and exhibit responses. In this work, the doping of graphene promoted the oriented adsorption of NO_2 molecules and decreased the optimal working temperature of NO_2 sharply. At such low temperature, the hybrid couldn't exhibit response to all VOCs. For other gases such as Cl_2, SO_2, and NH_3, their responses were also suppressed a lot compared with those at their respective optimal working temperature. As a result, the sensor based on 2.4% rGO-Co_3O_4 in this work exhibited excellent selectivity to NO_2 at room temperature.

4. Conclusions

We have successfully synthesized a series of porous Co_3O_4 slices/graphene hybrids through a facile two-step method. Moreover, we have explored the effect of graphene doping on the sensing performances in detail. We found that the hybrid with different doping amount of graphene possessed different sensing performances. Among them, 2.4% rGO-Co_3O_4 behaved the best, which exhibited a high response, fast response speed, excellent selectivity and long-term stability at RT. We attribute the enhanced gas sensing performance mainly to the larger surface area, enhanced O_C and O_V percentages and the coupling effect between the Co_3O_4 and graphene. Therefore, we can confirm that the doping of graphene is a promising strategy for realizing the detection of the Co_3O_4-based gas sensors to oxidizing gases such as NO_2. We believe our work can pave the way for other researchers to explore more high-performance Co_3O_4-based gas sensors toward NO_2 in the future.

Acknowledgments

This work was supported by the National Nature Science Foundation of China (61304242, 61520106003), National High-Tech Research and Development Program of China (863 Program, No. 2014AA06A505), Science and Technology Development Program of Jilin Province (No. 20150520091JH).

Appendix A. Supplementary data

Supplementary data associated with this article can be found, in the online version, at https://doi.org/10.1016/j.snb.2018.02.117.

References

[1] N. Hongsith, E. Wongrat, T. Kerdcharoen, S. Choopun, Sensor response formula for sensor based on ZnO nanostructures, Sens. Actuators B 144 (2010) 67–72.
[2] X.W. Li, X. Zhou, H. Guo, C. Wang, J.Y. Liu, P. Sun, F.M. Liu, G.Y. Lu, Design of Au@ZnO yolk-shell nanospheres with enhanced gas sensing properties, ACS Appl. Mater. Interfaces 6 (2014) 18661–18667.
[3] L.L. Wang, Z. Lou, J.N. Deng, R. Zhang, T. Zhang, Ethanol gas detection using a yolk-shell (core-shell) α-Fe_2O_3 nanospheres as sensing material, ACS Appl. Mater. Interfaces 7 (2015) 13098–13104.
[4] Y.Z. Li, Y.L. Cao, D.Z. Jia, Y. Wang, J. Xie, Solid-state chemical synthesis of mesoporous α-Fe_2O_3 nanostructures with enhanced xylene-sensing properties, Sens. Actuators B 198 (2014) 360–365.
[5] R.Q. Xing, L. Xu, Y.S. Zhu, J. Song, W.F. Qin, Q.L. Dai, D.L. Liu, H.W. Song, Three-dimensional ordered SnO_2 inverse opals for superior formaldehyde gas-sensing performance, Sens. Actuators B 188 (2013) 235–241.
[6] P. Sun, Y.S. Yu, J. Xu, Y.F. Sun, J. Ma, G.Y. Lu, One-step synthesis and gas sensing characteristics of hierarchical SnO_2 nanorods modified by Pd loading, Sens. Actuators B 160 (2011) 244–250.
[7] F.L. Gong, Y.Y. Gong, H.Z. Liu, M.L. Zhang, Y.H. Zhang, F. Li, Porous In_2O_3 nanocuboids modified with Pd nanoparticles for chemical sensors, Sens. Actuators B 223 (2016) 384–391.
[8] P. Song, D. Han, H.H. Zhang, J. Li, Z.X. Yang, Q. Wang, Hydrothermal synthesis of porous In_2O_3 nanospheres with superior ethanol sensing properties, Sens. Actuators B 196 (2014) 434–439.
[9] Y. Yao, F.X. Ji, M.L. Yin, X.P. Ren, Q. Ma, J.Q. Yan, S.Z.F. Liu, Ag nanoparticle-sensitized WO_3 hollow nanosphere for localized surface plasmon enhanced gas sensors, ACS Appl. Mater. Interfaces 8 (2016) 18165–18172.
[10] D.L. Chen, L. Yin, L.F. Ge, B.B. Fan, R. Zhang, J. Sun, G.S. Shao, Low-temperature and highly selective NO-sensing performance of WO_3 nanoplates decorated with silver nanoparticles, Sens. Actuators B 185 (2013) 445–455.
[11] J.H. Kim, A. Katoch, S.W. Choi, S.S. Kim, Growth and sensing properties of networked p-CuO nanowires, Sens. Actuators B 212 (2015) 190–195.
[12] S. Steinhauer, E. Brunet, T. Maier, G.C. Mutinati, A. Köck, Suspended CuO nanowires for ppb level H_2S sensing in dry and humid atmosphere, Sens. Actuators B 186 (2013) 550–556.
[13] C. Wang, J.Y. Liu, Q.Y. Yang, P. Sun, Y. Gao, F.M. Liu, J. Zheng, G.Y. Lu, Ultrasensitive and low detection limit of acetone gas sensor based on W-doped NiO hierarchical nanostructure, Sens. Actuators B 220 (2015) 59–67.
[14] J.M. Choi, J.H. Byun, S.S. Kim, Influence of grain size on gas-sensing properties of chemiresistive p-type NiO nanofibers, Sens. Actuators B 227 (2016) 149–156.
[15] H. Jin, Y.J. Huang, J.W. Jian, Plate-like Cr_2O_3 for highly selective sensing of nitric oxide, Sens. Actuators B 206 (2015) 107–110.
[16] J. Cao, Y.M. Xu, L.L. Sui, X.F. Zhang, S. Gao, X.L. Cheng, H. Zhao, L.H. Huo, Highly selective low-temperature triethylamine sensor based on Ag/Cr_2O_3 mesoporous microspheres, Sens. Actuators B 220 (2015) 910–918.
[17] S. Vetter, S. Haffer, T. Wagner, M. Tiemann, Nanostructured Co_3O_4 as a CO gas sensor: temperature-dependent behavior, Sens. Actuators B 206 (2015) 133–138.
[18] J.N. Deng, R. Zhang, L.L. Wang, Z. Lou, T. Zhang, Enhanced sensing performance of the Co_3O_4 hierarchical nanorods to NH_3 gas, Sens. Actuators B 209 (2015) 449–455.
[19] M.E. Franke, T.J. Koplin, U. Simon, Metal and metal oxide nanoparticles in chemiresistors: does the nanoscale matter? Small 2 (2006) 36–50.
[20] N. Barsan, D. Koziej, U. Weimar, Metal oxide-based gas sensor research: how to? Sens. Actuators B 121 (2007) 18–35.
[21] N. Yamazoe, G. Sakai, K. Shimanoe, Oxide semiconductor gas sensors, Catal. Surv. Asia 7 (2003) 63–75.
[22] H.J. Kim, H.M. Jeong, T.H. Kim, J.H. Chung, Y.C. Kang, J.H. Lee, Enhanced ethanol sensing characteristics of In_2O_3-decorated NiO hollow nanostructures via modulation of hole accumulation layers, ACS Appl. Mater. Interfaces 6 (2014) 18197–18204.
[23] J.W. Yoon, H.J. Kim, I.D. Kim, J.H. Lee, Electronic sensitization of the response to C_2H_5OH of p-type NiO nanofibers by Fe Doping, Nanotechnology 24 (2013) 1–8.
[24] H.J. Kim, J.H. Lee, Highly sensitive and selective gas sensors using p-type oxide semiconductors: overview, Sens. Actuators B 192 (2014) 607–627.
[25] M. Hübner, C.E. Simion, A.T. Stanoiu, S. Pokhrel, N. Bârsan, U. Weimar, Influence of humidity on CO sensing with p-type CuO thick film gas sensors, Sens. Actuators B 153 (2011) 347–353.
[26] S. Vetter, S. Haffer, T. Wagner, M. Tiemann, Nanostructured Co_3O_4 as a CO gas sensor: temperature-dependent behavior, Sens. Actuators B 206 (2015) 133–138.
[27] X.W. Xie1, Y. Li, Z.Q. Liu, M. Haruta, W.J. Shen, Low-temperature oxidation of CO catalysed by Co_3O_4 nanorods, Nature 458 (2009) 746–749.

[28] L.F. Liotta, H.J. Wu, G. Pantaleoa, A.M. Venezia, Co_3O_4 nanocrystals and Co_3O_4-MO_x binary oxides for CO, CH_4 and VOC oxidation at low temperatures: a review, Catal. Sci. Technol. 3 (2013) 3085–3102.
[29] Z.B. Zhuang, W.C. Sheng, Y.S. Yan, Synthesis of monodispere Au@Co_3O_4 core-shell nanocrystals and their enhanced catalytic activity for oxygen evolution reaction, Adv. Mater. 26 (2014) 3950–3955.
[30] D.P. Cai, D.D. Wang, B. Liu, L.L. Wang, Y. Liu, H. Li, Y.R. Wang, Q.H. Li, T.H. Wang, Three-dimensional Co_3O_4@$NiMoO_4$ core/shell nanowire arrays on Ni foam for electrochemical energy storage, ACS Appl. Mater. Interfaces 6 (2014) 5050–5055.
[31] W.H. Tan, J.F. Tan, L. Li, M.H. Dun, X.T. Huang, Nanosheets-assembled hollowed-out hierarchical Co_3O_4 microrods for fast response/recovery gas sensor, Sens. Actuators B 249 (2017) 66–75.
[32] B.F. Wu, L.L. Wang, H.Y. Wu, K. Kan, G. Zhang, Y. Xie, Y. Tian, L. Li, K.Y. Shi, Templated synthesis of 3D hierarchical porous Co_3O_4 materials and their NH_3 sensor at room temperature, Microporous Mesoporous Mater. 225 (2016) 154–163.
[33] J.J. Zhang, Y.Q. Liang, J. Mao, X.J. Yang, Z.D. Cui, S.L. Zhu, Z.Y. Li, 3D microporous Co_3O_4-carbon hybrids biotemplated from butterfly wings as high performance VOCs gas sensor, Sens. Actuators B 235 (2016) 420–431.
[34] Y.B. Cao, F.L. Yuan, M.S. Yao, J.H. Bang, J.H. Lee, A new synthetic route to hollow Co_3O_4 octahedra for supercapacitor applications, CrystEngComm 16 (2014) 826–833.
[35] J.M. Xu, J.P. Cheng, The advances of Co_3O_4 as gas sensing materials: a review, J. Alloys Compd. 686 (2016) 753–768.
[36] Y. Seekaew, D. Phokharatkul, A. Wisitsoraat, C. Wongchoosuk, Highly sensitive and selective room-temperature NO_2 gas sensor based on bilayer transferred chemical vapor deposited graphene, Appl. Surf. Sci. 404 (2017) 357–363.
[37] W.J. Yuan, A.R. Liu, L. Huang, C. Li, G.Q. Shi, High-performance NO_2 sensors based on chemically modified graphene, Adv. Mater. 25 (2013) 766–771.
[38] Y.R. Choi, Y.G. Yoon, K.S. Choi, J.H. Kang, Y.S. Shim, Y.H. Kim, H.J. Chang, J.H. Lee, C.R. Park, S.Y. Kim, H.W. Jang, Role of oxygen functional groups in graphene oxide for reversible room-temperature NO_2 sensing, Carbon 91 (2015) 178–187.
[39] E.C. Mattson, K. Pande, S. Cui, M. Weinert, J.H. Chen, C.J. Hirschmugl, Investigation of NO_2 adsorption on reduced graphene oxide, Chem. Phys. Lett. 622 (2015) 86–91.
[40] X. Liu, J.B. Sun, X.T. Zhang, Novel 3D graphene aerogel-ZnO composites as efficient detection for NO_2 at room temperature, Sens. Actuators B 211 (2015) 220–226.
[41] Y.L. Dong, X.F. Zhang, X.L. Cheng, Y.M. Xu, S. Gao, H. Zhao, L.H. Huo, Highly selective NO_2 sensor at room temperature based on nanocomposites of hierarchical nanosphere-like α-Fe_2O_3 and reduced graphene oxide, RSC Adv. 4 (2014) 57493–57500.
[42] X. Liu, J.W. Li, J.B. Sun, X.T. Zhang, 3D Fe_3O_4 nanoparticle/graphene aerogel for NO_2 sensing at room temperature, RSC Adv. 5 (2015) 73699–73704.
[43] B. Zhang, J. Liu, X.B. Cui, Y.L. Wang, Y. Gao, P. Sun, F.M. Liu, K. Shimanoe, N. Yamazoe, G.Y. Lu, Enhanced gas sensing properties to acetone vapor achieved by α-Fe_2O_3 particles ameliorated with reduced graphene oxide sheets, Sens. Actuators B 241 (2017) 904–914.
[44] W.T. Koo, S. Yu, S.J. Choi, J.S. Jang, J.Y. Cheong, I.D. Kim, Nanoscale PdO catalyst functionalized Co_3O_4 hollow nanocages using MOF templates for selective detection of acetone molecules in exhaled breath, ACS Appl. Mater. Interfaces 9 (2017) 8201–8210.
[45] S.L. Bai, L. Du, J.H. Sun, R.X. Luo, D.Q. Li, A.F. Chen, C.C. Liu, Preparation of reduced graphene oxide/Co_3O_4 composites and sensing performance to toluene at low temperature, RSC Adv. 6 (2016) 60109–60116.
[46] J.J. Zhang, Y.Q. Liang, J. Mao, X.J. Yang, Z.D. Cui, S.L. Zhu, Z.Y. Li, 3D microporous Co_3O_4-carbon hybrids biotemplated from butterfly wings as high performance VOCs gas sensor, Sens. Actuators B 235 (2016) 420–431.
[47] L. Li, M.M. Liu, S.J. He, W. Chen, Freestanding 3D mesoporous Co_3O_4@Carbon foam nanostructures for ethanol gas sensing, Anal. Chem. 86 (2014) 7996–8002.
[48] Y.L. Wang, J. Liu, X.B. Cui, Y. Gao, J. Ma, Y.F. Sun, P. Sun, F.M. Liu, X.S. Liang, T. Zhang, G.Y. Lu, NH_3 gas sensing performance enhanced by Pt-loaded on mesoporous WO_3, Sens. Actuators B 238 (2017) 473–481.
[49] X.Y. Zhu, Y.C. Guo, H. Ren, C. Gao, Y. Zhou, Enhancing the NO_2 gas sensing properties of rGO/SnO_2 nanocomposite films by using microporous substrates, Sens. Actuators B 248 (2017) 560–570.
[50] G.H. Lu, L.E. Ocola, J.H. Chen, Gas detection using low-temperature reduced graphene oxide sheets, Appl. Phys. Lett. 94 (2009) 1–4.
[51] H.Y. Jeong, D.S. Lee, H.K. Choi, D.H. Lee, J.E. Kim, J.Y. Lee, W.J. Lee, S.O. Kim, S.Y. Choi, Flexible room-temperature gas sensors based on carbon nanotubes/reduced graphene hybrid films, Appl. Phys. Lett. 96 (2010) 1–4.
[52] N. Chen, X.G. Li, X.Y. Wang, J. Yu, J. Wang, Z.N. Tang, S.A. Akbar, Enhanced room temperature sensing of Co_3O_4-intercalated reduced graphene oxide based gas sensors, Sens. Actuators B 188 (2013) 902–908.
[53] J. Zhang, J.J. Wu, X.X. Wang, D.W. Zeng, C.S. Xie, Enhancing room-temperature NO_2 sensing properties via forming heterojunction for NiO-rGO composited with SnO_2 nanoplates, Sens. Actuators B 243 (2017) 1010–1019.
[54] J.Z. Ou, W.Y. Ge, B. Carey, T. Daeneke, A. Rotbart, W. Shan, Y.C. Wang, Z.Q. Fu, A.F. Chrimes, W. Wlodarski, S.P. Russo, Y.X. Li, K. Kalantar-zadeh, Physisorption-based charge transfer in two-dimensional SnS_2 for selective and reversible NO_2 gas sensing, ACS Nano 9 (2015) 10313–10323.
[55] M. Donarelli, S. Prezioso, F. Perrozzi, F. Bisti, M. Nardone, L. Giancaterini, C. Cantalini, L. Ottaviano, Response to NO_2 and other gases of resistive chemically exfoliated MoS_2-based gas sensors, Sens. Actuators B 207 (2015) 602–613.
[56] R. Kumar, N. Goel, M. Kumar, UV-activated MoS_2 based fast and reversible NO_2 Sensor at room temperature, ACS Sens. 2 (2017) 1744–1752.
[57] S.L. Bai, J.W. Hu, D.Q. Li, R.X. Luo, A.F. Chen, C.C. Liu, Quantum-sized ZnO nanoparticles: synthesis, characterization and sensing properties for NO_2, J. Mater. Chem. 21 (2011) 12288–12294.
[58] R.J. Oweis, B.A. Albiss, M.I.A. Widyan, M.A.A. Akhras, Hybrid zinc oxide nanorods/carbon nanotubes composite for nitrogen dioxide gas sensing, J. Electron. Mater. 43 (2014) 3222–3228.
[59] C.Y. Lee, S.J. Kim, I.S. Hwang, J.H. Lee, Glucose-mediated hydrothermal synthesis and gas sensing characteristics of WO_3 hollow microspheres, Sens. Actuators B 142 (2009) 236–242.
[60] S.J. Choi, H.J. Choi, W.T. Koo, D.H. Huh, H. Lee, I.D. Kim, Metal-organic framework-templated PdO-Co_3O_4 nanocubes functionalized by SWCNTs: improved NO_2 reaction kinetics on flexible heating film, ACS Appl. Mater. Interfaces 9 (2017) 40593–40603.
[61] J.S. Lee, A. Katoch, J.H. Kim, S.S. Kim, Effect of Au nanoparticle size on the gas-sensing performance of p-CuO nanowires, Sens. Actuators B 222 (2016) 307–314.
[62] X.Q. Jie, D.W. Zeng, J. Zhang, K. Xu, J.J. Wu, B.K. Zhu, C.S. Xie, Graphene-wrapped WO_3 nanospheres with room-temperature NO_2 sensing induced by interface charge transfer, Sens. Actuators B 220 (2015) 201–209.
[63] X. Liu, J.S. Cui, J.B. Sun, X.T. Zhang, 3D graphene aerogel-supported SnO_2 nanoparticles for efficient detection of NO_2, RSC Adv. 4 (2014) 22601–22605.
[64] A.S.M.I. Uddin, D.T. Phan, G.S. Chung, Low temperature acetylene gas sensor based on Ag nanoparticles-loaded ZnO-reduced graphene oxide hybrid, Sens. Actuators B 207 (2015) 362–369.
[65] X. Li, J. Wang, D. Xie, J.L. Xu, Y. Xia, L. Xiang, Enhanced p-type NO_2-sensing properties of ZnO nanowires utilizing CNTs electrode, Mater. Lett. 206 (2017) 18–21.
[66] N. Yamazoe, New approaches for improving semiconductor gas sensors, Sens. Actuators B 5 (1991) 7–19.
[67] H.Y. Zhang, S. Pokhrel, Z.X. Ji, H. Meng, X. Wang, S.J. Lin, C.H. Chang, L.J. Li, R.B. Li, B.B. Sun, M.Y. Wang, Y.P. Liao, R. Liu, T. Xia, L. Madler, A.E. Nel, PdO doping tunes band-gap energy levels as well as oxidative stress responses to a Co_3O_4 p-type semiconductor in cells and the lung, J. Am. Chem. Soc. 136 (2014) 6406–6420.
[68] P.V. Kumar, M. Bernardi, J.C. Grossman, The impact of functionalization on the stability, work function, and photoluminescence of reduced graphene oxide, ACS Nano 7 (2013) 1638–1645.
[69] S.J. Choi, H.J. Choi, W.T. Koo, D.H. Huh, H. Lee, I.D. Kim, Metal-organic framework-templated PdO-Co_3O_4 nanocubes functionalized by SWCNTs: improved NO_2 reaction kinetics on flexible heating film, ACS Appl. Mater. Interfaces 9 (2017) 40593–40603.
[70] Y.Y. Liang, Y.G. Li, H.L. Wang, J.G. Zhou, J. Wang, T. Regier, H.J. Dai1, Co_3O_4 nanocrystals on graphene as a synergistic catalyst for oxygen reduction reaction, Nat. Mater. 10 (2011) 780–786.
[71] W. Zeng, T.M. Liu, Gas-sensing properties of SnO_2-TiO_2-based sensor for volatile organic compound gas and its sensing mechanism, Phys. B 405 (2010) 1345–1348.
[72] A.P. Lee, B.J. Reedy, Temperature modulation in semiconductor gas sensing, Sens. Actuators B 60 (1999) 35–42.

Biographies

Bo Zhang received the BE degree in College of Chemistry from Jilin University in 2013. He is currently working toward the Dr. degree in College of Electronic Science and Engineering, Jilin University. His research interests include the synthesis of graphene and its applications in gas sensors.

Ming Cheng received his BE degree from Jilin University of China in 2017. He is currently working toward the MS degree in the Electronics Science and Engineering department, Jilin University. His current researches focus on the preparation and application of graphene and semiconductor oxide, especially in gas sensor.

Guannan Liu received his BE degree from Jilin University of China in 2015. He is currently working toward the MS degree in the Electronics Science and Engineering department, Jilin University. His current researches focus on the synthesis of carbon dots and their applications.

Yuan Gao received her PhD degree from Department of Analytical Chemistry at Jilin University in 2012. Now she is an associate professor in Jilin University, China. Her current researches focus on the preparation and application of graphene and semiconductor oxide, especially in gas sensor and biosensor.

Lianjing Zhao received her MS degree from Jilin University of China in 2013. She is currently working toward the Ph.D. degree in the Electronics Science and Engineering department, Jilin University. Her research interests mainly focus on the on the development of the functional nanomaterials for biosensors.

Shan Li is presently studying the MS degree in the Electronics Science and Engineering department, Jilin University. Her research directions involve fabrication of mesoporous oxide semiconductor and their applications in gas sensors.

Yipei Wang enrolls as an undergraduate student in Jilin University, majoring in Electronic Information Science and Engineering. She is currently focusing on the research of Electronic Circuit and System.

Fangmeng Liu received his PhD degree in 2017 from College of Electronic Science and Engineering, Jilin University, China. Now he is a lecturer of Jilin University, China. His current research interests include the application of functional materials and development of solid state electrolyte gas sensor and flexible device.

Xishuang Liang received the B.Eng. degree in Department of Electronic Science and Technology in 2004. He received his Doctor's degree in College of Electronic Science and Engineering at Jilin University in 2009. Now he is an associate professor of Jilin University, China. His current research is solid electrolyte gas sensor.

Tong Zhang completed her MS degree in semiconductor materials in 1992 and her PhD in the field of microelectronics and solid-state electronics in 2001 from Jilin University. She was appointed as a full-time professor in the College of Electronics Science and Engineering, Jilin University in 2001. Her research interests are sensing functional materials, gas sensors, humidity sensors and electrochemical sensors.

Geyu Lu received the B. Sci. degree in electronic sciences in 1985 and the M. Sci. degree in 1988 from Jilin University in China and the Dr. Eng. degree in 1998 from Kyushu University in Japan. Now he is a professor of Jilin University, China. His current research interests include the development of chemical sensors and the application of the function materials.